American Mineralogist, Volume 84, pages 1061–1070, 1999

The surface structure of α-Fe_2O_3 (001) by scanning tunneling microscopy: Implications for interfacial electron transfer reactions

CARRICK M. EGGLESTON*

Department of Geology and Geophysics, University of Wyoming, Laramie, Wyoming 82071-3006, U.S.A.

ABSTRACT

STM images of hematite (α-Fe_2O_3) (001) surfaces taken under a wider variety of conditions than in previous studies are presented. The results strongly suggest that only Fe sites contribute to the tunneling current. Specifically, corrugated unit-cell structures expected of the Fe sublattice are observed under both occupied- and unoccupied-states imaging conditions. A pattern of apparent vacancies was observed under conditions previously attributed to oxygen states; this is most simply interpreted either as Fe vacancies, or Fe sites whose electronic structure has been altered by a (unknown) coordinating anion, but difficult to explain as the oxygen sublattice. For unoccupied states imaging, decreasing the tip-sample distance (increasing the tunneling current) results in an image change from only one site per unit cell to three sites per unit cell. This is also relatively easy to explain using the Fe sublattice, but difficult to explain using the oxygen sublattice. These results are modeled using resonant tunneling theory, which shows that changes in bias voltage, tunneling medium, and tip-sample distance can have the observed effects only if Fe atoms are being imaged. The results have implications for modeling electron transfer across mineral-water interfaces more generally because they provide a framework for understanding site-specific electron transfer kinetic parameters.

INTRODUCTION

The structure and reactivity of iron oxide surfaces is of interest not only for technological and industrial purposes (Jansen et al. 1995; Condon et al. 1994; Gaines et al. 1997; Tarrach et al. 1993; Wasserman et al. 1997; Wang et al. 1998; Wiesendanger et al. 1992), but also for the many natural processes in which they participate. Iron oxide surfaces are sorbents for aqueous solutes (e.g., Dzombak and Morel 1990; Hug 1997; Kallay and Matijevic 1985) and electron donors or acceptors in thermal (Afonso et al. 1990; Afonso and Stumm 1992; LaKind and Stone 1989; Suter et al. 1991; Zinder et al. 1986), photoelectrochemical (Anderman and Kennedy 1988; Faust et al. 1989; Sulzberger et al. 1989; Waite and Morel 1984) and biological (Dobbin et al. 1996; Grantham and Dove 1996; Grantham et al. 1997; Lovley 1991; Lovley and Phillips 1988; Nealson and Myers 1992) electron transfer processes.

Studies of Al and Fe oxide surfaces by low energy electron diffraction (LEED) and photoelectron spectroscopy revealed complex surface reconstructions and non-stoichiometry (see Eggleston and Hochella 1992; Henrich and Cox 1994; Kim et al. 1997 and references therein). The sputter-anneal cycles used to prepare clean, well-defined surfaces of single-element metals and other materials (e.g., Si, Au, Ge) were problematic for Fe, Al, and other oxides. For example, Condon et al. (1995) showed that an unusual phenomenon they called "biphase ordering," most likely a product of particular sample preparation conditions, is probably the cause of complex LEED patterns observed in earlier work. Recent work by Gao and Chambers (1997), Gao et al. (1997a, 1997b), and Kim et al. (1997) on growth of well-defined thin films of α-Fe_2O_3 is providing well-defined iron oxide surfaces for study by surface science methods.

Scanning tunneling microscopy (STM) has been applied to several iron oxides; here, only studies of hematite (α-Fe_2O_3) are discussed. Hochella et al. (1989) produced topographic images, and Heil et al. (1989) tentatively interpreted their image as showing oxygen positions. Eggleston and Hochella (1992) concluded that images showed the oxygen sublattice at negative (sample-to-tip; occupied states) bias and the uppermost Fe sublattice at positive (tip-to-sample, unoccupied states) bias. Condon et al. (1995, 1998) imaged α-Fe_2O_3 (001) in vacuum; the surface had been partly reduced to FeO (111) in the cleaning process, and they found biphase ordering in which areas of FeO (111)-like surface alternated in a periodic pattern (unit-cell size, 3.5 ± 0.3 nm) with areas of α-Fe_2O_3(001)-like surface. They interpreted the α-Fe_2O_3(001)-like areas as consistent with oxygen atoms, but could not rule out a contribution from Fe atoms. Wang et al. (1998) found two distinct surface domains in STM images of the (001) surface in vacuum, and proposed that they represent coexisting oxygen-terminated and iron-terminated (001) surface structures.

In the α-Fe_2O_3(001) surface structure, each type of Fe site has a different height relative to a (001) surface plane (Fig. 1). The uppermost ("A") Fe layer should relax significantly (50–60%) toward the surface in vacuum (Becker et al. 1996; Wang et al. 1998), but this effect is likely to be mitigated in aqueous solution or humid air where Fe coordination (tetrahedral and octahedral coordination have both been proposed; Wasserman

*E-mail: carrick@uwyo.edu

0003-004X/99/0708–1061$05.00

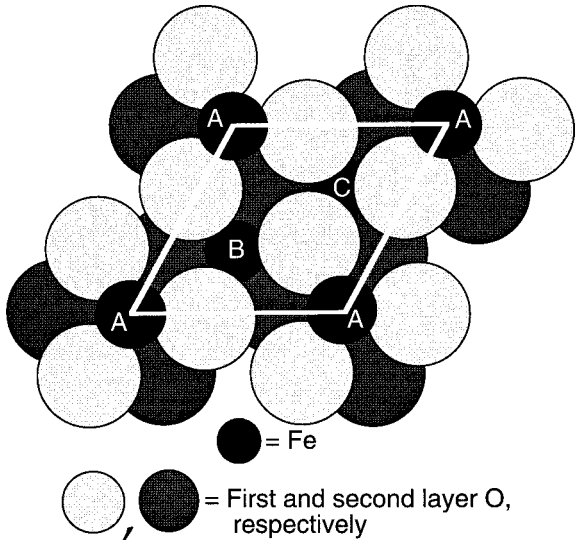

FIGURE 1. A simplified model of the hematite (001) surface. "Corrugated" unit cell is marked (edge length = 0.504 nm). In an unrelaxed hematite structure, "A" Fe atoms are 0.085 nm above, and "B" and "C" Fe atoms 0.085 and 0.145 nm below, respectively, the first oxygen layer. "A" Fe atoms are situated above vacancies in the underlying octahedral layer.

et al. 1997; Becker et al. 1996) is more complete than in vacuum. Because the Fe atoms occur at different heights, we might expect the great sensitivity of STM tunneling current to tip-sample distance to give images of a similarly "corrugated" pattern (i.e., different currents or heights associated with the different Fe types in Fig. 1) when imaging Fe atoms. However, this is probably not always the case.

Becker et al. (1996) reported ab-initio slab and cluster calculations of the relaxed structure, and calculated STM images, of the α–Fe_2O_3 (001) surface. They show that the tunneling current under negative bias conditions, assuming electrons tunnel from the valence band to the STM tip, can be dominated by either Fe or O state density depending on which specific site is involved. They show that O 2p like orbitals converge on threefold symmetry axes above Fe locations, so that even when tunneling current is dominated by O 2p state density, maximum tunneling current occurs over Fe locations. For positive sample bias, Fe atoms were the chief electron acceptors, but different Fe sites dominate the image with changes in tip-sample distance. Slab calculations by Wang et al. (1998) showed that Fe-terminated and an O-terminated (001) surfaces are possible, and that Fe 3d surface states can contribute significantly to surface chemistry in both cases.

This paper presents STM imaging of the α-Fe_2O_3 (001) surface, which suggest that previous interpretations of STM images may need revision and that Fe sites are the most important contributors to tunneling current in STM imaging of this surface. I also model the STM imaging of the α-Fe_2O_3 (001) surface using resonant tunneling theory (see, for example, Schmickler and Widrig 1992).

MATERIALS AND METHODS

STM

A Nanoscope III STM (Digital Instruments) was used to raster a sharp metal W tip over a conductive surface. This tip acts as an electron donor or acceptor for currents created by a bias voltage imposed between tip and sample. Application of the technique to minerals is reviewed by Eggleston (1994).

α-Fe_2O_3

The α-Fe_2O_3 samples from Mina Gerais, Brazil, were used in previous studies (Eggleston and Hochella 1992; Johnsson et al. 1991). The α-Fe_2O_3 specimens containing donor impurities are n-type semiconductors at low temperature because conduction band electrons are much more mobile as charge carriers than are valence band holes at room temperature (Goodenough 1972; Leland and Bard 1987; Anderman and Kennedy 1988; Merchant et al. 1979). Except where stated, all samples were imaged in air after immersion in water to help ensure that the surface was hydrated. Samples were dried by touching a Kimwipe the crystal edge to wick bulk water away.

Because of drift and other problems (Eggleston 1994), STM is an imprecise way to measure interatomic distances. The unit-cell dimension on the α-Fe_2O_3 (001) surface, based on X-ray diffraction, is 0.504 nm (Blake et al. 1966; Sato and Akimoto

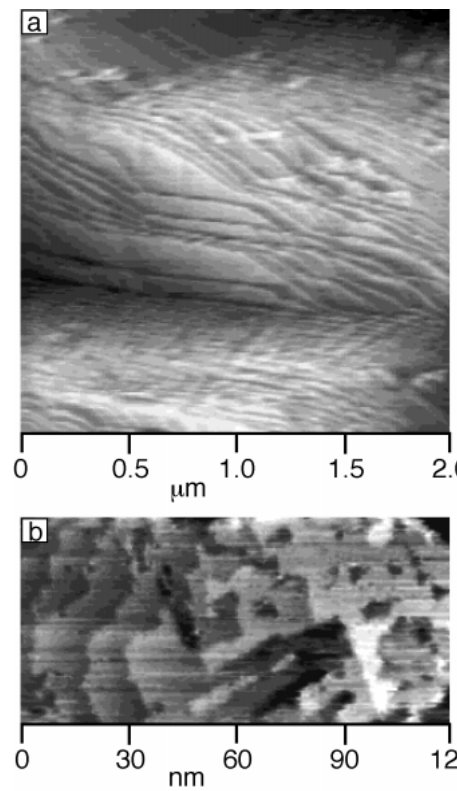

FIGURE 2. (a) Image taken at –721.7 mV, 729 pA. Step density is 30 μm^{-1} or more in places, equivalent to about 30 nm terrace width. **(b)** Topographical image of a fracture surface taken at –387.1 mV, 1.02 nA. Steps at left are measured at 0.24 nm high, similar to the expected 0.23 nm step height.

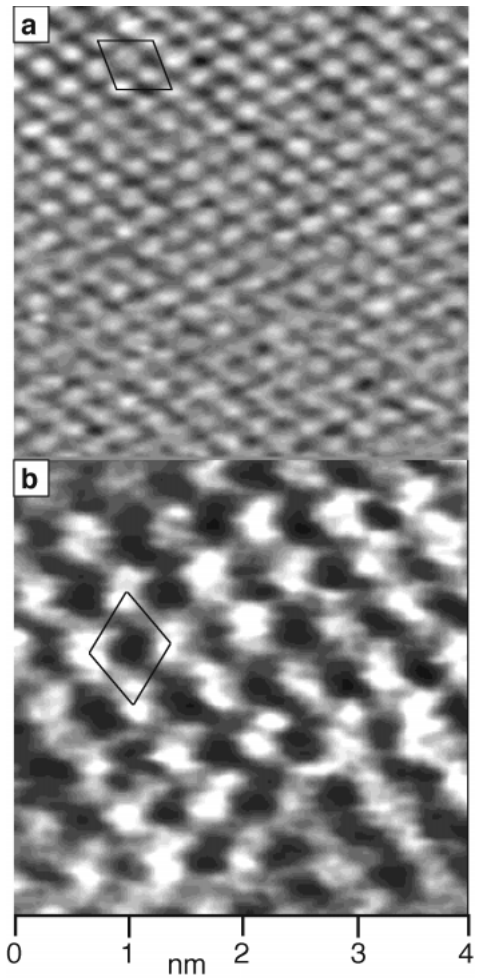

FIGURE 3. STM images taken in oil. **(a)** Occupied-states image with hexagonal periodicity of ~0.3 nm (–335.6 mV, 1.03 nA). Current contrast = 500 pA. **(b)** Unoccupied-states image with hexagonal periodicity of ~0.5 nm (+900 mV, 1.53 nA). Current contrast = 800 pA. In later figures, the current contrast expressed in the image grayscale is referred to as the "grayscale."

1979), but for simplicity we refer to this periodicity in STM images as the "0.5 nm" structure, and to the nominally 0.295 nm periodicity of the oxygen sublattice (and of the Fe sublattice if differences in vertical position are ignored, which will be useful later) as the "0.3 nm" structure.

RESULTS

Microtopography

Hematite parts along (001). Fracture surfaces nominally parallel to (001) are not very flat (Fig. 2). Terraces were rarely more than 3 nm wide. Because of this, together with scanner creep and thermal drift, it was not possible to obtain STM images of atomically ordered terraces much larger than those presented here. This paper focuses on the ordered α-Fe_2O_3 (001) surface, so steps are not considered.

Atomic-scale images

Reproduction of previous results. STM by Eggleston and Hochella (1992) used α-Fe_2O_3 surfaces created by fracture in oil. As discussed below, the presence of oil is a key difference between their images and later images taken under "wet" conditions (e.g., in humid air or in air after exposure of the surface to aqueous solution). Figure 3 shows STM results similar to those of Eggleston and Hochella (1992). For negative bias (tunneling from occupied states of the surface to the tip, Fig. 3a), a uniform, hexagonal array with 0.3 nm periodicity is seen. This result, consistently obtained, led to an interpretation of the images as states associated with oxygen ions. For positive bias (tunneling from the tip to unoccupied states of the surface, Fig. 3b), a hexagonal pattern with 0.5 nm periodicity is seen, i.e., that expected for any one, but not all, of the three types of Fe atoms in Figure 1.

Occupied-states images. In Figures 4 and 5, a corrugated 0.5 nm unit cell (e.g., Fig. 1) is seen instead of the uniform 0.3 nm periodicity typified by Figure 3a and previously reported for occupied states images (Eggleston and Hochella 1992). Corrugated unit cells are observed at both –320 mV and –548.1 mV (Figs. 4 and 5); Figure 6 is a two-dimensional fast Fourier transform (2DFFT) of Figure 5a, showing the 0.3 nm and 0.5 nm periods found in the image. The highest-current sites in Figures 4 and 5 cannot necessarily be equated with "A-type"

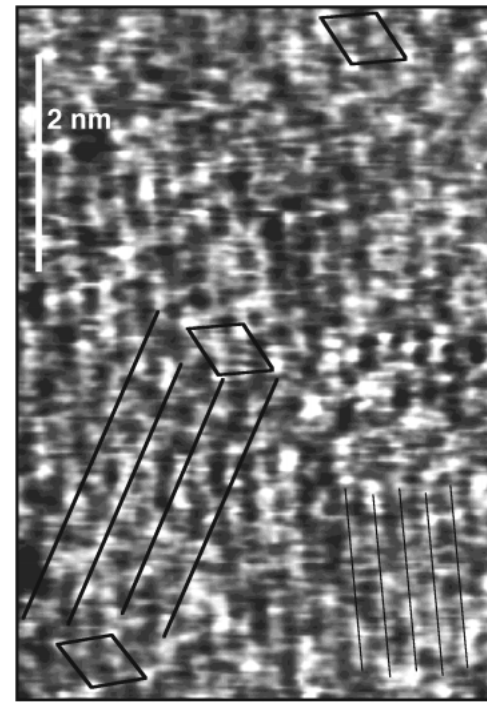

FIGURE 4. A noisy image (low-pass filtered; –320 mV, 1.09 nA, grayscale = 90 pA) displaying a 0.5 nm periodicity (heavy black lines) rotated 30° relative to a 0.3 nm periodicity (thin black lines), a relationship expected for the "corrugated" unit cell (Fig. 1). Three examples are given of unit cells that are qualitatively consistent (despite noise) with the iron sublattice.

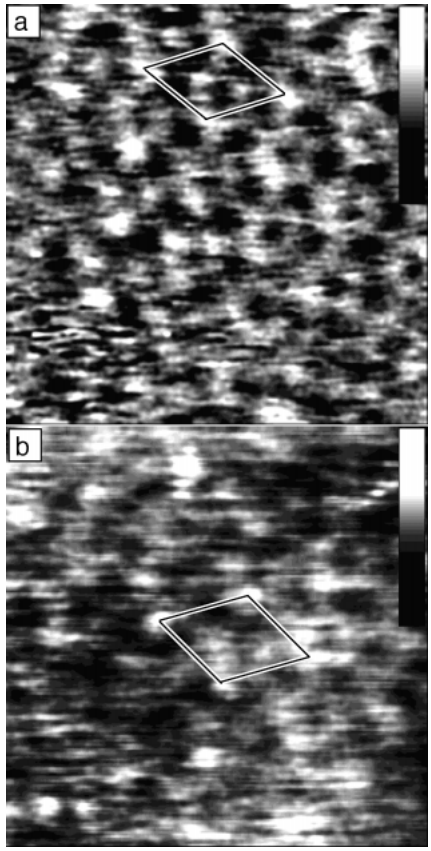

FIGURE 5. Two images taken at –548.1 mV, 264 pA. **(a)** Grayscale = 80 pA. **(b)** Grayscale = 180 pA. In both images, a corrugated unit cell (Fig. 1) is marked (edge length ~5nm).

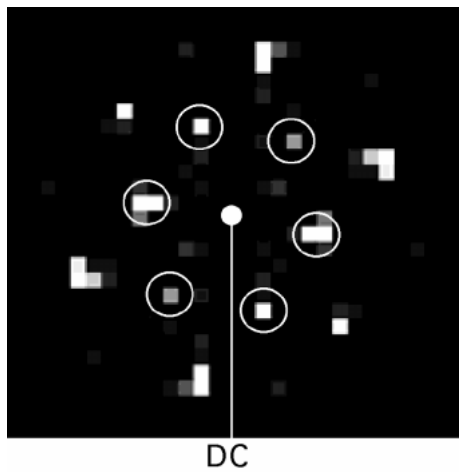

FIGURE 6. A 2DFFT of Figure 5a. The white dot at center is the low frequency (DC) limit; the Nyquist limit is 0.095 nm. The grayscale corresponds to the magnitude of the FFT at a given radial frequency; circled peaks correspond to a radial frequency of about 0.3 nm, and uncircled peaks correspond to a radial frequency of about 0.5 nm. Both of these frequencies occur in a hexagonal pattern (distorted slightly by drift during imaging). The two patterns are rotated by 30° with respect to each other.

Fe atoms (Becker et al. 1996), as discussed below. Figure 7 shows a 0.3 nm periodicity in the upper part, but a pattern of vacancies with 0.5 nm periodicity in the lower part. This pattern has not previously been observed, although our interpretation of this image (see below) is similar to that of Wang et al. (1998). Condon et al. (1995, 1998) also observed a corrugated unit cell (Fig. 1). Thus, occupied-states images taken in vacuum and in air can both show a corrugated unit cell.

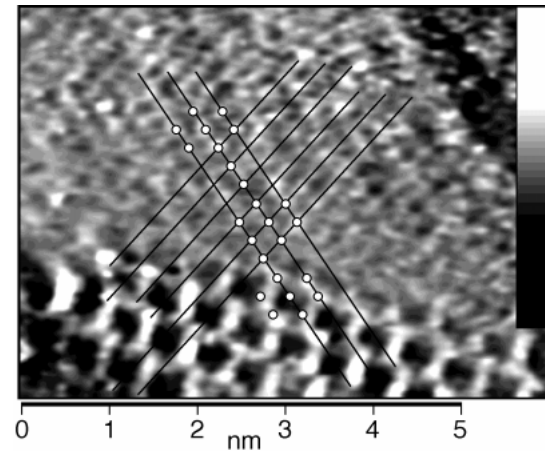

FIGURE 7. STM image taken at –340.0 mV, 941.5 pA; grayscale = 858 pA, lowpass filtered. The upper part of the image shows a (noisy) 0.3 nm periodicity, and the lower part shows a 0.5 nm pattern of vacancies consistent with imaging of a single octahedral layer of Fe positions (i.e., only "B" and "C" sites from Fig. 1). Note that the hexagonal pattern has been compressed in the y direction by drift. Lines and dots demonstrate that the two parts of the image are commensurate.

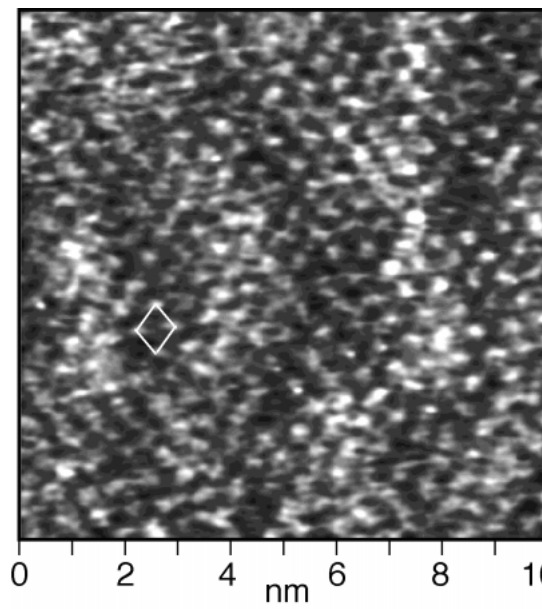

FIGURE 8. STM image (+900 mV, 1.52 nA) of 0.5 nm periodicity (unoccupied states). Gray tone in image corresponds to 600 pA.

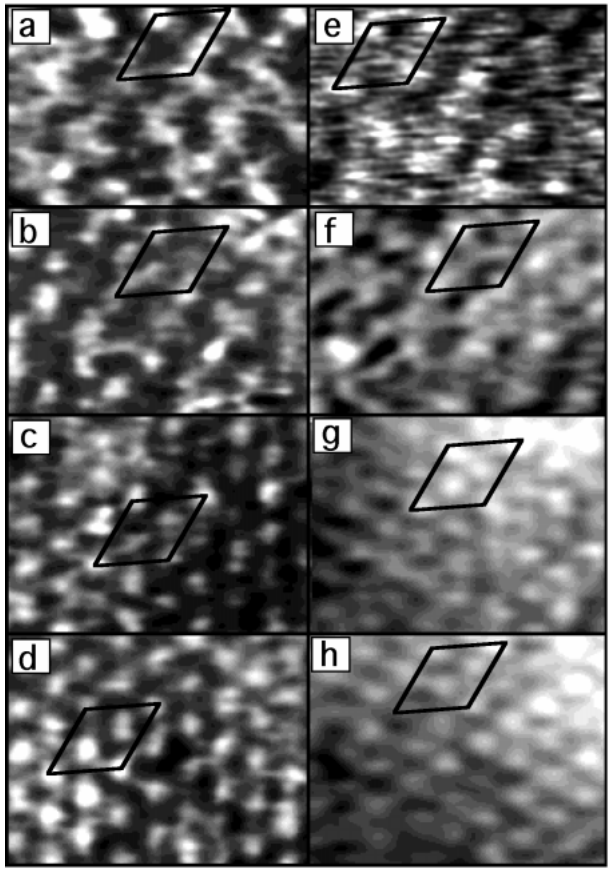

FIGURE 9. STM images of current contrast **(a–d)** and tip height **(e–h)** as a function of tunneling current, all at +1.15 V bias. Conditions in order of setpoint current and grayscale in nA are: **(a)** 5.0, 0.8; **(b)** 10.7, 2.3; **(c)** 19.7, 4.1; **(d)** 28.0, 6.6. Conditions in order of setpoint current in nA and grayscale in nm are: **(e)** 4.8, 0.1; **(f)** 10.1, 0.1; **(g)** 19.0, 0.1; **(h)** 32.2, 0.1. Example unit cells are marked.

Unoccupied-states images. Many of our positive-bias STM images are similar to Figure 3b. A wider-area (10×10 nm) example is given in Figure 8. However, other images, particularly of steps, showed both the 0.5 and 0.3 nm periodicities in different parts of single images. Also, Becker et al. (1996) calculated unoccupied-states STM images in which image characteristics vary as a function of tip-sample distance. At a tip-sample distance of 0.25 nm, the calculated image emphasizes the "A" Fe sites (see Fig. 1), whereas at a tip-sample distance of 0.4 nm, the "B" Fe sites are emphasized (we thus cannot say which Fe site is being imaged in Figs. 3B or 8). Prompted by these experimental and computational indications, images were made as a function of tunneling current (higher current = smaller tip-sample distance; Fig. 9). Figure 10 gives corresponding 2DFFTs.

With the tip relatively far from the surface, both the 0.3 and 0.5 nm periodicities are seen (Fig. 9a and 9e for current and height data, respectively and Fig. 10a for the 2DFFT). As the setpoint current is increased (to very high values for which the tip field could alter surface electronic structure; McEllistrem et al. 1993, Schmickler and Widrig 1992), the 0.5 nm periodicity gives way to a 0.3 nm periodicity. Figure 10b–d shows the disappearance of the low frequency FFT peaks. Thus, images identical to those obtained at negative bias can be obtained for positive bias as well. Unfortunately, due to drift, we cannot be sure which site corresponds to which between the different parts of Figure 9. These results show that by varying imaging parameters, one can obtain all of the previously observed image types (0.3 nm, 0.5 nm, and "corrugated" unit cells).

INTERPRETATION AND DISCUSSION

Implications of results

The results presented here differ from those of Eggleston and Hochella (1992), but are similar to those of Condon et al. (1995, 1998) and Wang et al. (1998). Here, imaging is done in air, whereas Eggleston and Hochella (1992) used a nonaqueous oil medium and Condon et al. (1995) and Wang et al. (1998) imaged in vacuum. As shown below, different media could indeed give different images. Here, it is argued that all of these images show only Fe locations, based on the following observations.

(1) It is difficult to explain a corrugated 0.5 nm unit cell (e.g., Figs. 4 and 5) as purely related to the oxygen sublattice because all of the oxygen sites at the (001) surface are symmetrically equivalent. However, if there is a contribution from Fe states (Becker et al. 1996), a corrugated unit cell is possible.

(2) The lattices in the upper and lower parts of Figure 7 are commensurate. There is no obvious change in altitude to suggest a step or phase change at the border between the different surface patterns. The lower part of Figure 7 might be explained simply by removing A-type Fe (Fig. 1) from over-vacancy sites such that only Fe sites within a single octahedral layer (i.e., only B- and C-type Fe sites; Fig. 1) are imaged. Such a surface structure has been calculated to be stable in vacuum at high oxygen partial pressures by Wang et al. (1998). Another possibility is that the ability of the A-type Fe atoms to transmit current is decreased for an unknown reason. A regular removal of oxygen atoms, or regular substitution by a foreign anion, is highly unlikely.

(3) Corrugated unit cells are seen in both occupied- and unoccupied-states images. The corrugated pattern is thus not unique to unoccupied-states images.

(4) The bias voltages used in this study ranged from –550 mV to 1150 mV, spanning only 1.7 eV in energy. This is significantly smaller than the 2.2 eV bulk bandgap of α-Fe_2O_3. Surface states could narrow the surface bandgap, and the presence of the STM tip could also have an effect (McEllistrem et al. 1995), but narrowing of the surface bandgap by 0.5 eV is unlikely. One interpretation of this, therefore, is that the negative-bias images do not show the valence band, or that the positive-bias images do not show the conduction band.

Hematite is an n-type semiconductor for which charge transport occurs via electron hopping from Fe site to Fe site (Anderman and Kennedy 1988; Gao et al. 1997a; Goodenough 1972; Merchant et al. 1979; Sieber et al. 1985). This fact, together with the foregoing observations, suggests that the tunneling current in the STM images either comes from (occupied-states images) or

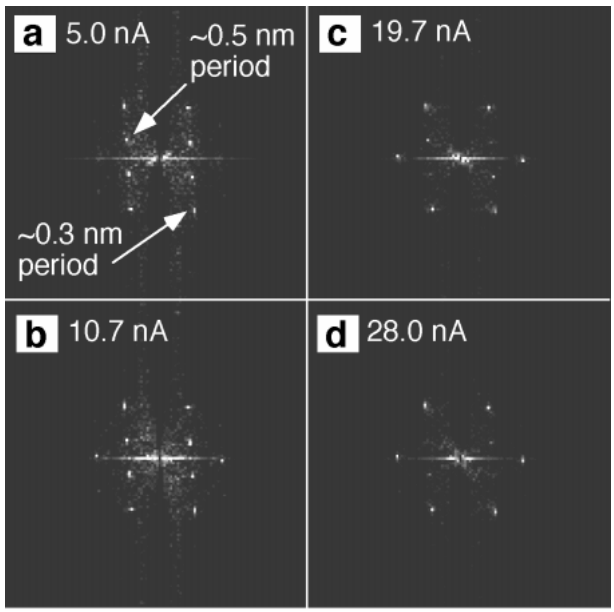

FIGURE 10. 2DFFTs corresponding to the images in Figure 9a–d. In **(a)**, the ~0.3 and ~0.5 nm periods are marked.

goes to (unoccupied-states images) Fe states of the α-Fe_2O_3 conduction band. Below, STM images calculated on the basis of resonant tunneling theory are presented to test this proposal.

Resonant tunneling

Schmickler (1993, 1995) and Schmickler and Widrig (1992) formulated a theory of resonant tunneling through redox centers positioned between an electrode surface and an STM tip (Fig. 11). This approach is used here to interpret analogous electron transfer between an STM tip and bulk α-Fe_2O_3 via unoccupied Fe states at the surface.

An oxidized redox center ("Ox" in Fig. 11a) can accept electrons from an electrode and donate them to the tip, and vice versa. Because this center is relatively close, and therefore better coupled electronically (i.e., better overlap of donor and acceptor states) to both the substrate and the tip compared to the longer tip-substrate distance, current through the redox center can dominate an image (Schmickler and Widrig 1992). The situation is analogous for Fe^{3+} at the α-Fe_2O_3 surface (Fig. 11b). B- and C-type Fe sites are closely coupled to the underlying bulk, but are relatively poorly coupled to the tip. In contrast, A-type Fe sites are poorly coupled to the bulk, but more closely coupled to the tip. Qualitatively, this suggests that height differences could appear to "even out" in an STM image because Fe sites at different heights simply trade weak coupling on one side for stronger coupling on the other, the net current changing little. This might serve as an explanation for images (e.g., Figs. 3a, 9d and 9h) in which all sites appear at more or less the same current (or height). However, A-type Fe sites have different energies associated with their lowermost unoccupied states as compared to B- and C-type Fe sites (as well as other differences) that complicate this simple picture.

Following Schmickler and Widrig (1992), the current density associated with the situation illustrated in Figure 11a is:

$$j = -e_0 \frac{\pi}{h} \int_0^{eV_b} \rho_s(\varepsilon)\rho_t(\varepsilon) \frac{|V_{sr}|^2 |U_{rt}|^2}{\Delta} D_{ox}(\varepsilon) d\varepsilon \qquad (1)$$

where e_0 is electron charge, $\hbar$ is Planck's constant, the integral runs over energy ε from 0 to eV_b where V_b is bias voltage; $\rho_s(\varepsilon)$ and $\rho_t(\varepsilon)$ are the density of states (DOS) of the substrate and tip, respectively; and V_{sr} and U_{rt} are matrix elements for electron transfer between substrate and redox center, and redox center and tip, respectively (i.e., they are transition probabilities that depend on orbital shape, overlap, relative energies, and spin state). The symbol Δ describes broadening of the redox center's electronic states by interaction with the substrate (such broadening is more important for redox centers adsorbed on the surfaces of metallic conductors than for wide bandgap semiconductors; Schmickler 1995). $D_{ox}(\varepsilon)$ is the density of oxidized (unoccupied) states on the redox center and in the limit $\Delta = 1$ (no broadening, the case used here), is given by

$$D_{ox}(\varepsilon) = \sqrt{\frac{\pi}{kT\lambda}} \exp\left[\frac{-(\varepsilon - \varepsilon_r)^2}{4\lambda kT}\right] \qquad (2)$$

where λ is a solvent-dependent reorganization energy for the redox center, and ε_r is the energy level of the unoccupied state on the redox center (for Fe^{3+}, ε_r is the energy level of the lowest unoccupied Fe 3d orbital that can accept electrons). Equation 2 imposes a Gaussian distribution on the density of oxidized (unoccupied) states for the redox center (Gerischer 1960). The width of the distribution increases, and the amplitude decreases, as λ increases. As shown by Schmickler and Widrig (1992), Δ in Equation 1 has an effect very similar to λ in Equation 2; it broadens the effective DOS distribution.

Equations 1 and 2 couple a classical treatment of nuclear motion with a quantum mechanical treatment of electron motion. Reorganization and relaxation of solvent structure generally must occur upon electron transfer (Marcus 1965, 1990; Marcus and Sutin 1985). For example, because Fe^{2+}-O bonds are longer than Fe^{3+}-O bonds, it takes significant energy (~2.6 eV) to reorganize H_2O molecules around Fe^{2+} and Fe^{3+} ions in response to electron transfers to or from them in aqueous solution (e.g., Graetzel 1989). The corresponding reorganization of lattice ions around Fe centers within α-Fe_2O_3 is much smaller; Goodenough (1972) has estimated a value of 0.3 eV. Indeed, this is a key observation. Because large effective λ for a given redox center increases the activation energy and thus slows the rate of electron transfer to and from that center, electron transfer involving the site with the highest effective λ will be rate-limiting in a series reaction. Thus, because λ is largest for surface Fe sites as compared to either the hematite bulk or the STM tip, surface Fe sites should form the "bottleneck" in electron transfer through the interface (i.e., from the hematite bulk, through surface Fe sites, and into the STM tip in series) and resonant tunneling theory should be applicable.

It may be questioned whether the space between the hematite and the STM tip is sufficient for free solvent reorganization. While λ should be affected by the presence of the STM tip, the excellent experimental study by Tao (1996) shows that a measure of λ can be obtained from Fe atoms situated be-

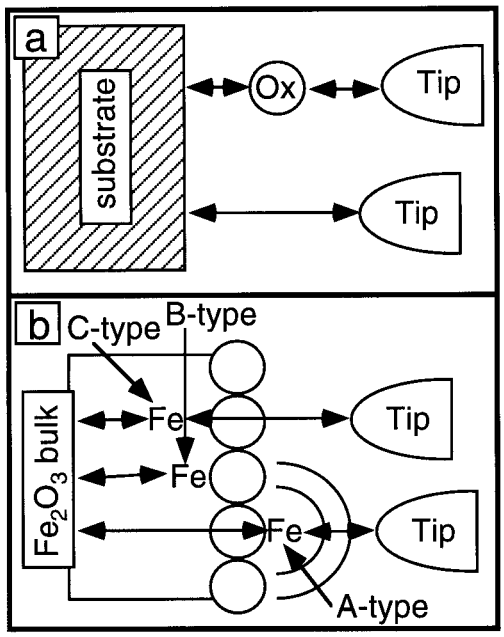

FIGURE 11. (a) Illustration of the resonant tunneling concept. A redox center with unoccupied states, "Ox", can accept electrons from a substrate electrode and donate them to the tip, and vice versa. **(b)** Fe atoms at the α-Fe_2O_3 (001) surface are treated analogously to the situation in **a**; see text for details.

tween a graphite electrode and an STM tip, strongly supporting the applicability of resonant tunneling theory to STM imaging of surface Fe redox centers.

Equation 1 can be recast as follows (Schmickler and Widrig 1992):

$$j = -e_0 \frac{\pi}{h} \int_0^{eV_b} AT_{sr}(\varepsilon) BT_{rt}(\varepsilon) D_{ox}(\varepsilon) d\varepsilon \qquad (3)$$

where

$$\rho_s(\varepsilon)\,|V_{sr}|^2 = AT_{sr}(\varepsilon)$$
$$\rho_s(\varepsilon)\,|U_{rt}|^2 = BT_{rt}(\varepsilon) \qquad (4)$$

A and *B* are the portion of the DOS and coupling matrix elements that are not distance dependent. The tunneling probabilities T_{ij} (where the indexes ij are equal to either sr or rt in Equations 3 and 4) can be expressed (Gamow 1928) as $T_{ij} = \exp[-\beta_{ij} d_{ij}]$, where β_{ij} is a decay constant whose exact value depends on knowledge of the shape and height of the local potential barrier to electron tunneling in the medium of interest between the ij donor-acceptor pair separated by distance d_{ij}. For specific Fe sites at the α-Fe_2O_3 (001) surface, β is not known, but for electron transfers to and from d orbitals in transition metals (Co and Mn) β varies from 1.3 to 2.4 $Å^{-1}$ (Graetzel 1989). As discussed by Schmickler and Widrig (1992), direct electron transfer from the substrate to the STM tip (in our case, from Fe centers deeper than those illustrated in Fig. 1) is generally negligible compared to the current through the redox centers, and is neglected in the images calculated (see below) on the basis of Equation 3.

Because molecular reorganization is key to the resonant tunneling approach, the frequency of electron transmission through Fe centers should be much lower than the vibrational frequency of Fe-O bonds so that there is time for reorganization to take place between electron transfers. A typical vibrational frequency at 298 K is 6.21×10^{12}/s (kT/h). In comparison to this vibrational frequency, the frequency of electron transmission through a surface Fe site at a tunneling current of 1 nA is equivalent to 6.24×10^9 electrons/s. A current of 40 nA is equivalent 2.5×10^{11} electrons/s. Thus, the electron transmission frequency is about three orders of magnitude lower than kT/h in all cases except for the higher currents in Figure 9.

Calculated images

Here, no attempt is made to calculate the DOS and matrix element parameters needed to quantify A, B, ρ_t, ρ_s, β_{ij}, and ε_r for Equation 3. Ab-initio or semi-empirical calculations of these parameters is a subject for future work. Instead, these parameters are adjusted to give reasonable currents for desired "baseline" images. Then we ask: what is the effect on images of changing λ, bias voltage, or tip-surface distance?

The α-Fe_2O_3 Fermi level is positioned at the bottom of the conduction band. Becker et al. (1996) show that A-type sites have most of their DOS at higher energy than B- or C-type sites relative to the conduction band edge, and have a surface state below the conduction band edge within the bulk bandgap. However, because the energies of these states from Becker et al. (1996) are not applicable to non-vacuum conditions and not easily amenable to application within Equation 3, we choose 0.4 and –0.1 eV as a reasonable approximation for the energy levels (ε_r) of these two parts of the A-type DOS above and below the Fermi level, respectively. B- and C-type Fe sites are assigned $\varepsilon_r = 0.1$ eV. β terms for all Fe-tip interactions are assigned a value of 2.0 $Å^{-1}$, and A and B are taken as unity.

For comparison purposes, we adjust the β values for Fe-substrate interactions, for a bias voltage of –300 mV and 3.0 Å tip-sample distance, until images similar to Figure 3a are obtained. We then change the voltage and λ parameters to see how they affect this baseline image. Similarly, for positive bias voltage (+400 mV), we adjust β values until images similar to Figure 9d are obtained, and then vary the tip-sample distance.

To examine the consequences of a change in medium from oil to air (with adsorbed water at the surface due to water vapor in the air) between Eggleston and Hochella (1992) and this study, we must choose reorganizations energies (λ) applicable to both media (Table 1). We take λ for bulk hematite as 0.3 eV (Goodenough 1972), and for bulk oil to be slightly larger (0.5 eV). We use the previously cited value of 2.6 eV for λ in bulk water. We use only the outer sphere component of this value (1.1eV; Graetzel 1989) for λ for B- and C-type Fe sites because these sites do not have any inner-sphere water as a solvent. Values are given in Table 1.

Figure 12 gives the calculated images. Figures 12a–d show the effect of increasing the bias voltage from –200 mV to –500 mV for imaging in oil (intended to approximate conditions used by Eggleston and Hochella 1992). The corresponding image changes from an emphasis on B- and C-type Fe sites to A-type Fe sites because the different Fe sites have different DOS dis-

tributions as a function of energy, so that different amounts of the DOS are sampled from each type of site at different bias voltages. In the midrange voltages, there is a point at which all Fe sites appear at about the same current (Fig. 12b), similar to Figure 3a. This is our baseline image.

The similarity between Figure 12a and the experimental result in the lower part of Figure 7 shows that a region of apparent A-type Fe vacancies can also be interpreted as region in which A-type Fe sites are coordinated by (unknown) molecules that alter local electronic structure or λ values.

Figure 12e gives the result of changing only the λ values from Figure 12b to those characteristic of water. In water, the image emphasizes A-type Fe sites (B- and C-type Fe sites also occur, but are much smaller and are lost within the dark part of the grayscale, similar to Fig. 12d only more so). Figures 12f–h show the effect of decreasing the tip-surface distance. This result is comparable to the experimental results in Figure 9. Figure 12i shows the effect of changing λ values from those for water in Figure 12h to those for oil; there is little change in this case, probably because +400 mV exactly coincides with the ε_r value chosen for A-type Fe sites.

It is inadvisable to read too much into the calculated images. The ad-hoc nature of choosing values for A, B, ρ_t, ρ_s, β_{ij}, and ε_r means that any specific result could be different, depending on the relative magnitudes chosen for these parameters. Thus, the differences between, for example, Figs. 12 f–h and the results of Becker et al. (1996) may only reflect differences in the DOS at a given energy between the two calculations. We lack both the detailed electronic structure (DOS, matrix elements, β values) information and the extensive, systematic experimental data needed to more rigorously test the applicability of resonant tunneling theory to hematite STM imaging. Nevertheless, it is clear from Figure 12 that changing λ values (i.e., changing imaging medium from vacuum to oil or to water) can have a significant impact on image characteristics, as can the different electronic structure of A-type vs. B- and C-type Fe sites.

CONCLUSIONS

STM images of α-Fe_2O_3 (001) surfaces are consistent with imaging Fe locations and are qualitatively consistent with a resonant tunneling model. A more quantitative treatment must await quantum mechanical calculations of needed parameters and should account for the effect of different tunneling media and of STM-imposed surface electric fields on the local electronic structure.

The results suggest that a more rigorous treatment will be worthwhile. Organic coatings on iron or other oxide minerals

TABLE 1. Reorganization energies λ used in resonant tunneling calculations (eV)

Medium	Bulk Fe_2O_3	Bulk oil	A-type	B-type	C-type
Oil	0.3	0.5	0.5*	0.4†	0.4†
H_2O	0.3	2.6	1.45‡	0.75§	0.75§

*A-type sites assumed dominated by "oil-like" λ.
†Values assume an average between bulk and oil λ.
‡Value from 0.5(0.3) + 0.5(2.6).
§Value from 0.5(0.3) + 0.5(1.1).

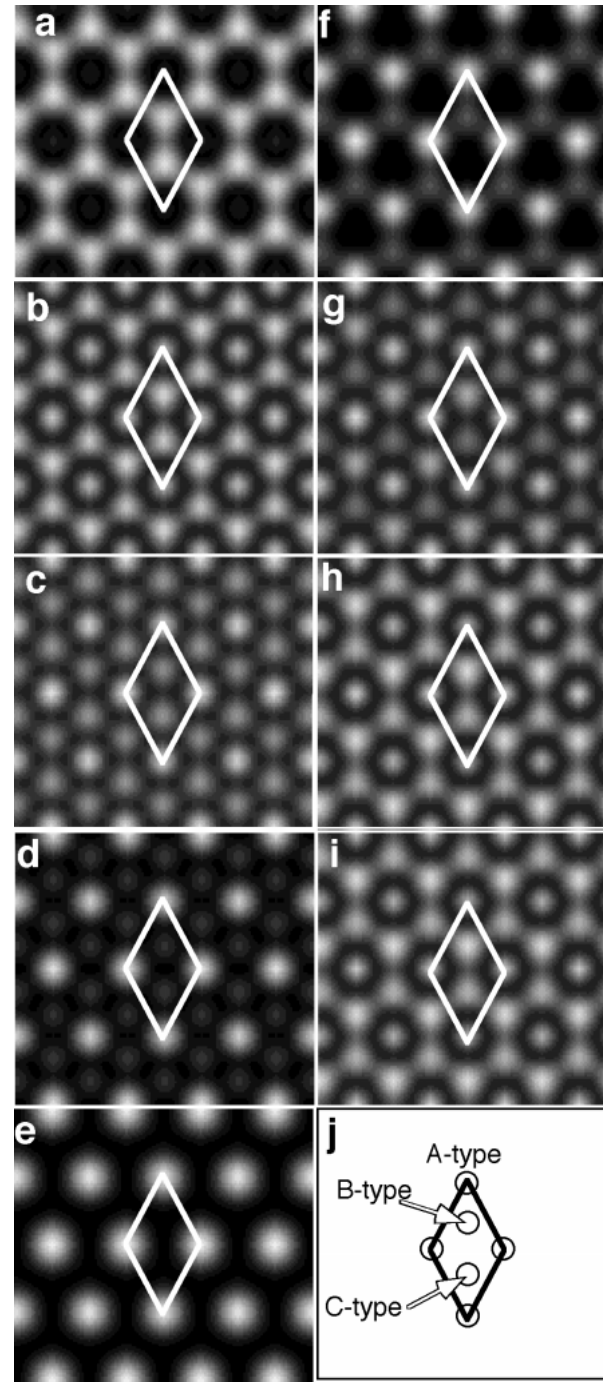

FIGURE 12. Calculated STM images based on Equation 3 and Table 1. Parameters are listed below are respectively bias voltage (mV), average current (nA), current corrugation (maximum-minimum; nA), tip-surface distance (Å) where zero distance is taken as the z position of A-type Fe atoms, and medium for which λ values are applicable. **(a)** –200, 0.873, 0.33, 3, oil; **(b)** –300, 0.968, 0.23, 3, oil; **(c)** –400, 0.974, 0.028, 3, oil; **(d)** –500, 0.968, 0.42, 3, oil; **(e)** –300, 0.968, 0.23, water, 3; **(f)** 400, 0.628, 0.36, 3, water; **(g)** 400, 3.71, 0.356, 2, water; **(h)** 400, 8.83, 1.30, 1.5, water; **(i)** 400, 8.83, 1.29, 1.5, oil; **(j)** illustration of how the three different types of Fe sites relate to the unit cell drawn in each image.

(e.g., oxides of Ti or Mn) are likely to have profound effects on electron transfer kinetics, and it may be possible to rationalize and systematize such effects within a resonant tunneling framework. This study is a first step toward a better understanding of how specific mineral surface sites interact with surrounding media to change interfacial electron transfer kinetics. For example, iron-reducing bacteria may gain a kinetic advantage in their use of Fe^{3+} at mineral surfaces as a terminal electron acceptor by coating the surface with organic material and decreasing the effective λ for electron transfer. It might be possible to design organic coatings or films that promote the ability of iron metal grains in iron filings walls to reductively dehalogenate halocarbons migrating in groundwater (Matheson and Tratnyek 1994). Finally, judicious and systematic STM imaging of hematite (or other oxide) surfaces under controlled electrochemical conditions may allow us to measure local DOS as a function of energy and thus to gain a better quantitative understanding of in-situ surface electronic structure.

ACKNOWLEDGMENTS

This work was supported by NSF EPSCoR-9550477 and NSF EAR-9634143. The manuscript benefitted greatly from reviews by U. Becker, J. Rustad, and S. Stipp.

REFERENCES CITED

Afonso, M.D.S. and Stumm, W. (1992) Reductive dissolution of iron(III) (hydr)oxides by hydrogen sulfide. Langmuir, 8, 1671–1675.

Afonso, M.D.S., Morando, P.J., Blesa, M.A., Banwart, S., and Stumm, W. (1990) The reductive dissolution of iron oxides by ascorbate. Journal of Colloid and Interface Science, 138(1), 74–82.

Anderman, M. and Kennedy, J.H. (1988) Iron Oxide (Fe_2O_3). In H.O. Finklea, Ed., Semiconductor Electrodes, 55, p. 147–202. Elsevier, Amsterdam.

Becker, U., Hochella, M.F. Jr., and Apra, E. (1996) The electronic structure of hematite {001} surfaces: Applications to the interpretation of STM images and heterogeneous surface reactions. American Mineralogist, 81, 1301–1314.

Blake, R.L., Hessevick, R.E., Zoltai, T., and Finger, L.W. (1966) Refinement of the hematite structure. American Mineralogist, 51, 123–129.

Condon, N.G., Murray, P.W., Leibsle, F.M., Thornton, G., Lennie, A.R., and Vaughan, D.J. (1994) Fe_3O_4(111) termination of α-Fe_2O_3(0001). Surface Science Letters, 310, L609–L613.

Condon, N.G., Leibsle, F.M., Lennie, A.R., Murray, P.W., Vaughan, D.J., and Thornton, G. (1995) Biphase ordering of iron oxide surfaces. Physical Review Letters, 75, 1961–1964.

Condon, N.G., Leibsle, F.M., Lennie, A.R., Murray, P.W., Parker, T.M., Vaughan, D.J., and Thornton, G. (1998) Scanning tunneling microscopy studies of α-Fe_2O_3(0001). Surface Science, 397, 278–287.

Dobbin, P.S., Requena Burmeister, L.M., Heath, S.L., Powell, A.K., McEwan, A.G., and Richardson, D.J. (1996) The influence of chelating agents upon the dissimilatory reduction of Fe(III) by Shewanella putrefaciens. Part 2. Oxo- and hydroxo-bridged polynuclear Fe(III) complexes. BioMetals, 9, 291–301.

Dzombak, D.A. and Morel, F.M.M. (1990) Surface Complexation Modeling. Wiley, New York.

Eggleston, C.M. (1994) High-resolution scanning probe microscopy: Tip-surface interaction, artifacts, and applications in mineralogy and geochemistry. In K.L. Nagy, and A.E. Blum, Eds., Scanning Probe Microscopy of Clay Minerals, 7, 1–90. Clay Minerals Society, Boulder, Colorado.

Eggleston, C.M. and Hochella, M.F. Jr. (1992) The structure of hematite (001) surfaces by scanning tunneling microscopy: Image interpretation, surface relaxation, and step structure. American Mineralogist, 77, 911–922.

Faust, B.C., Hoffmann, M.R., and Bahnemann, D.W. (1989) Photocatalytic oxidation of sulfur dioxide in aqueous suspensions of α-Fe_2O_3. Journal of Physical Chemistry, 93, 6371–6381.

Gaines, J.M., Bloemen, P.J.H., Kohlhepp, J.T., Bulle-Lieuwma, C.W.T., Wolf, R.M., Reinders, A., Jungblut, R.M., van der Heiden, P.A.A., van Eemeren, J.T.W.M., aan de Stegge, J., and De Jonge, W.J.M. (1997) An STM study of Fe3O4(100) grown by molecular beam epitaxy. Surface Science, 373, 85–94.

Gamow, G. (1928) The quantum theory of the atom nucleus. Zeitschrift für Physik, 51, 204–212.

Gao, Y. and Chambers, S.A. (1997) Heteroepitaxial growth of α-Fe_2O_3, γ-Fe_2O_3 and Fe_3O_4 thin films by oxygen-plasma-assisted molecular beam epitaxy. Journal of Crystal Growth, 174, 446–454.

Gao, Y., Kim, Y.J., Chambers, S.A., and Bai, G. (1997a) Synthesis of epitaxial films of Fe_3O_4 and α-Fe_2O_3 with various low-index orientations by oxygen-plasma-assisted molecular beam epitaxy. Journal of Vacuum Science and Technology, 15, 332–339.

Gao, Y., Kim, Y.J., Thevuthasan, S., and Chambers, S.A. (1997b) Growth, structure, and magnetic properties of γ-Fe_2O_3 epitaxial films on MgO. Journal of Applied Physics, 81, 3253–3256.

Gerischer, H. (1960) Uber den Ablauf von Redoxreaktionen an Metallen und an Halbleitern II. Metall-Elektroden. Zeitschrift Für Physikalishe Chemie Neue Folge, 26, 325–338.

Goodenough, J.B. (1972) Metallic oxides. Progress in Solid State Chemistry, 5, 145–399.

Graetzel, M. (1989) Heterogeneous Photochemical Electron Transfer. 159 p. CRC Press, Inc., Boca Raton, Florida.

Grantham, M.C. and Dove, P.M. (1996) Investigation of bacterial-mineral interactions using Fluid Tapping Mode Atomic Force Microscopy. Geochimica et Cosmochimica Acta, 60, 2473–2480.

Grantham, M.C., Dove, P.M., and DiChristina, T.J. (1997) Microbially catalyzed dissolution of iron and aluminum oxyhydroxide mineral surface coatings. Geochimica et Cosmochimica Acta, 61(21), 4467–4477.

Heil, J., Wesner, B., Lommel, B., Assmus, W., and Grill, W. (1989) Structural investigation of surface of blue bronze and hematite by scanning tunneling microscopy. Journal of Applied Physics, 65(12), 5220–5222.

Henrich, V.E. and Cox, P.A. (1994) The Surface Science of Metal Oxides. Cambridge University Press, Cambridge.

Hochella, M.F. Jr., Eggleston, C.M., Elings, V.B., Parks, G.A., Brown, G.E. Jr., Wu, C.M., and Kjoller, K. (1989) Mineralogy in two dimensions: Scanning tunneling microscopy of semiconducting minerals with implications for geochemical reactivity. American Mineralogist, 74, 1233–1246.

Hug, S.J. (1997) In-Situ Fourier Transform Infrared Measurements of Sulfate Adsorption on Hematite in Aqueous Solutions. Journal of Colloid and Interface Science, 188, 415–422.

Jansen, R., Brabers, V.A.M., and van Kempen, H. (1995) One-dimensional reconstruction observed on Fe_3O_4(110) by scanning tunneling microscopy. Surface Science, 328, 237–247.

Johnsson, P.A., Eggleston, C.M., and Hochella, M.F. Jr. (1991) Imaging molecular-scale and microtopography of hematite with the atomic force microscope. American Mineralogist, 76, 1442–1445.

Kallay, N. and Matijevic, E. (1985) Adsorption at solid/solution interfaces. 1. Interpretation of surface complexation of oxalic and citric acids with hematite. Landmuir, 1, 195–201.

Kim, Y.J., Gao, Y., and Chambers, S.A. (1997) Selective growth and characterization of pure, epitaxial α-Fe_2O_3(0001) and Fe_3O_4(001) films by plasma-assisted molecular beam epitaxy. Surface Science, 371, 358–370.

LaKind, J.S. and Stone, A.T. (1989) Reductive dissolution of goethite by phenolic reductants. Geochimica et Cosmochimica Acta, 53, 961–971.

Leland, J.K. and Bard, A.J. (1987) Photochemistry of semiconducting iron oxide polymorphs. Journal of Physical Chemistry, 91, 5076–5083.

Lovley, D.R. (1991) Dissimilatory Fe(III) and Mn(IV) reduction. Microbiological Reviews, 55, 259–287.

Lovley, D.R. and Phillips, E.J.P. (1988) Novel mode of microbial energy metabolism: Organic carbon oxidation coupled to dissimilatory reduction of iron or manganese. Applied and Environmental Microbiology, 54, 1472–1480.

Marcus, R.A. (1965) On the theory of electron transfer reactions. VI. Unified treatment for homogeneous and electrode reactions. The Journal of Chemical Physics, 43, 679–701.

——(1990) Reorganization free energy for electron transfers at liquid-liquid and dielectric semiconductor-liquid interfaces. Journal of Physical Chemistry, 94, 1050–1055.

Marcus, R.A. and Sutin, N. (1985) Electron transfers in chemistry and biology. Biochimica et Biophysica Acta, 811, 265–322.

Matheson, L.J., and Tratnyek, P.G. (1994) Reductive dehalogenation of chlorinated methanes by iron metal. Environmental Science and Technology, 28, 2045–2053.

McEllistrem, M., Haase, G., Chen, D., and Hamers, R.J. (1993) Electrostatic sample-tip interactions in the scanning tunneling microscope. Physical Review Letters, 70, 2471–2474.

Merchant, P., Collins, R., Kershaw, R., Dwight, K., and Wold, A. (1979) The electrical, optical and photoconducting properties of $Fe_{2-x}Cr_xO3$ ($0 \le x \le 0.47$). Journal of Solid State Chemistry, 27, 307–315.

Nealson, K.H. and Myers, C.R. (1992) Microbial reduction of manganese and iron: New approaches to carbon cycling. Applied and Environmental Microbiology, 58, 439–443.

Sato, Y. and Akimoto, S. (1979) Hydrostatic compression of four corundum type compounds: α-Al_2O_3, V_2O_3, Cr_2O_3, and α-Fe_2O_3. Journal of Applied Physics, 50, 5285–5291.

Schmickler, W. (1993) Investigation of electrochemical electron transfer reactions with a scanning tunneling microscope: a theoretical study. Surface Science, 295, 43–56.

——(1995) The metal-solution interface in the STM-configuration. In A.A. Gewirth,

and H. Siegenthaler, Eds. Nanoscale Probes of the Solid/Liquid Interface, p. 5–24. Kluwer Academic Publishers, The Netherlands.

Schmickler, W. and Widrig, C. (1992) The investigation of redox reactions with a scanning tunneling microscope. Journal of Electroanalytical Chemistry, 336, 213–221.

Sieber, K.D., Sanchez, C., Turner, J.E., and Somorjai, G.A. (1985) Preparation, characterization and photoelectronic properties of germanium-substituted Fe_2O_3 single crystals. Faraday Transactions 1, 81, 1263–1274.

Sulzberger, B., Suter, D., Siffert, C., Banwart, S., and Stumm, W. (1989) Dissolution of Fe(III)(hydr)oxides in Natural Waters; Laboratory Assessment on the Kinetics Controlled by Surface Coordination. Marine Chemistry, 28, 127–144.

Suter, D., Banwart, S., and Stumm, W. (1991) Dissolution of hydrous iron(III) oxides by reductive mechanisms. Langmuir, 7, 809–813.

Tao, N.J. (1996) Probing potential-tuned resonant tunneling through redox molecules with scanning tunneling microscopy. Physical Review Letters, 76, 4066–4069.

Tarrach, G., Burgler, D., Schaub, T., Wiesendanger, R., and Guntherodt, H.J. (1993) Atomic surface structure of Fe_3O_4(001) in different preparation stages studied by scanning tunneling microscopy. Surface Science, 285, 1–14.

Waite, T.D. and Morel, F.M.M. (1984) Photoreductive dissolution of colloidal iron oxide: Effect of citrate. Journal of Colloid and Interface Science, 102, 121–137.

Wang, X.-G., Weiss, W., Shaikhutdinov, Sh.K., Ritter, M., Petersen, F., Wagner, F. Schlögl, R., and Scheffler, M. (1998) The hematite (α-Fe_2O_3) (0001) surface: Evidence for domains of distinct chemistry. Physical Review Letters 81, 1038–1041.

Wasserman, E., Rustad, J.R., Felmy, A.R., Hay, B.P., and Halley, J.W. (1997) Ewald methods for polarizable surfaces with application to hydroxylation and hydrogen bonding on the (012) and (001) surfaces of α-Fe_2O_3. Surface Science, 385, 217–239.

Wiesendanger, R., Shvets, I.V., Burgler, D., Tarrach, G., Guntherodt, H.J., Coey, J.M.D., and Graser, S. (1992) Topographic and magnetic-sensitive scanning tunneling microscope study of magnetite. Science, 255, 583–586.

Zinder, B., Furrer, G., and Stumm, W. (1986) The coordination chemistry of weathering: II. Dissolution of Fe(III) oxides. Geochimica et Cosmochimica Acta, 50, 1861–1869.

MANUSCRIPT RECEIVED JULY 27, 1998
MANUSCRIPT ACCEPTED FEBRUARY 2, 1999
PAPER HANDLED BY SUSAN L.S. STIPP